Exceptional Cluster of Simultaneous Shallow Landslides in Rwanda: Context, Triggering Factors, and Potential Warnings

Fils-Vainqueur Byiringiro, Marc Jolivet, Olivier Dauteuil, Damien Arvor, Christine Hitimana Niyotwambaza

GeoHazards

MDPI

Article

Exceptional Cluster of Simultaneous Shallow Landslides in Rwanda: Context, Triggering Factors, and Potential Warnings

Fils-Vainqueur Byiringiro [1], Marc Jolivet [1,*], Olivier Dauteuil [1], Damien Arvor [2] and Christine Hitimana Niyotwambaza [3]

[1] Centre National de la Recherche Scientifique (CNRS), Géosciences Rennes, ULR 6118, Université Rennes, F-35000 Rennes, France; fils-vainqueur.byiringiro@univ-rennes.fr (F.-V.B.); olivier.dauteuil@univ-rennes.fr (O.D.)
[2] Centre National de la Recherche Scientifique (CNRS), Laboratory Littoral–Environnement–Télédétection–Géomatique (LETG), UMR 6554, Université Rennes 2, F-35000 Rennes, France; damien.arvor@univ-rennes2.fr
[3] Ministry in Charge of Emergency Management (MINEMA), KN3 Rd, Kigali P.O. Box 4386, Rwanda; cniyotwambaza@minema.gov.rw
* Correspondence: marc.jolivet@univ-rennes1.fr

Abstract: Rwanda, in eastern tropical Africa, is a small, densely populated country where climatic disasters are often the cause of considerable damage and deaths. Landslides are among the most frequent hazards, linked to the country's peculiar configuration including high relief with steep slopes, humid tropical climate with heavy rainfall, intense deforestation over the past 60 years, and extensive use of the soil for agriculture. The Karongi region, in the west-central part of the country, was affected by an exceptional cluster of more than 700 landslides during a single night (6–7 May 2018) over an area of 100 km^2. We analyse the causes of this spectacular event based on field geological and geomorphology investigation and CHIRPS and ERA5-Land climate data. We demonstrate that (1) the notably steep slopes favoured soil instability; (2) the layered soil and especially the gravelly, porous C horizon allowed water storage and served as a detachment level for the landslides; (3) relatively low intensity, almost continuous rainfall over the previous two months lead to soil water-logging; and (4) acoustic waves from thunder or mechanical shaking by strong wind destabilized the water-logged soil through thixotropy triggering the landslides. This analysis should serve as a guide for forecasting landslide-triggering conditions in Rwanda.

Keywords: natural hazard; rainfall-induced landslides; eastern Africa; thunderstorms; high population density

Citation: Byiringiro, F.-V.; Jolivet, M.; Dauteuil, O.; Arvor, D.; Hitimana Niyotwambaza, C. Exceptional Cluster of Simultaneous Shallow Landslides in Rwanda: Context, Triggering Factors, and Potential Warnings. *GeoHazards* **2024**, *5*, 1018–1039. https://doi.org/10.3390/geohazards5040049

Academic Editor: Fabio Vittorio De Blasio

Received: 9 July 2024
Revised: 16 September 2024
Accepted: 21 September 2024
Published: 25 September 2024

1. Introduction

The worldwide growth in population leading to the constant occupation of poorly accessible lands (deserts, mountains, etc.) results in increased exposure to natural hazards [1]. This is further accentuated by global warming. While giant fires, floods, and droughts are becoming more and more devastating, landslides remain among the main hazards for local populations, especially in mountain areas [2]. With a surface of about 26,000 km^2 and a population of more than 13 million people, increasing about 2.3% per year [3], Rwanda is the most densely populated country in continental Africa (571 people per km^2). This small land-locked country of eastern-equatorial Africa, also known as the "Land of the Thousand Hills" for its hilly to mountainous landscape, is located along the geodynamic structure of the East African Rift System (Figure 1a). To the West, the Congo–Nile ridge (or Kivu Ridge) bordering Lake Kivu results from the extensional tectonic activity along the eastern edge of the Kivu graben that was initiated during the late Miocene [4,5]. The altitude of the Kivu Ridge ranges between 1500 m and 3000 m, and the slopes locally reach up to 60°. To the northwest, the Virunga volcanic belt notably includes Mount Kalisimbi (4507 m,

the summit of Rwanda) and the active Nyiragongo volcano in the Democratic Republic of Congo.

Because of its elevated topography (Figure 1b,c) and its geographic situation close to the Equator, Rwanda is subjected to a temperate tropical climate [6–8]. The Kivu Ridge acts as a topographic barrier for the moisture brought from the Indian Ocean by the easterly winds, leading to between 1300 and 1600 mm of orographic rainfall in western Rwanda (Figure 1d). The climate is characterized by two rainfall seasons, autumn (September to December) and late spring (March to May) separated by a less rainy period during two months (January and February) and a dry season (June to August). Since the 1960s, the constant increase in population associated with the scarcity of agricultural land has led to intensive deforestation and over-exploitation of the soil, especially in the Kivu region [9,10]. The steep topography, high rainfall, near-complete deforestation, intense degradation of the silt–clayey soil, and a major increase in population are all favouring a high level of landslide hazards. The landslide-related death toll has thus increased dramatically from 38 in the period 2011–2013 to 174 in the period 2013–2016 and 551 between 2016 and 2021 [11–14].

It is generally considered that rainfall is a main factor inducing shallow and deep landslide formation [15–18]. Short-time (a few hours to a few days) heavy rainfalls [19–21] and long-lasting (1 to 5 months) exceptional events [22,23] both play a role. However, the effect of those two rainfall patterns vary depending on the local geomorphology and soil type. Indeed, fine-grained soil with low permeability will require higher antecedent rainfall and permeable soil before the pore water pressure reaches its maximum [24]. In addition, long-term rainfall modifies soil properties, especially by forcing the migration of fine-grained material or dissolving and recrystallizing elements, modifying the porosity and permeability [25]. In that respect, daily rainfall (or even short-term, 1 to a few days rainfall) is not always a reliable parameter to predict landslides [17] as long-term continuous rainfall, allowing infiltration in poorly permeable soils, may be more efficient in reaching the pore water pressure threshold [18].

Research works on landslides in Rwanda were initiated in the late 1989s with some first descriptions of soil creeping and the impact of runoff water on slope stability [26,27]. These first studies were followed by a gap of several years, and only in 2014, did research start again, mainly based on remote sensing analysis. Most efforts consisted of building landslide occurrence and susceptibility maps in the country [28–32]. Although of main interest, those maps show remarkable differences mainly linked to the type of satellite images used, the data processing method, the restricted area investigated by the authors, and the limits in landslide size considered pertinent [28,29,33]. The mechanisms triggering and controlling the genesis of landslides in Rwanda have been less explored. Most authors consider that given the tropical humid climate, rainfall is the main driver [28,33–36]. Furthermore, no obvious correlation seems to exist with earthquakes generated by the Kivu Rift activity [37]. Few studies include field-based observations such as the nature and structure of the soil and substratum, the vegetation cover, the occurrence of previous landslides, and the infrastructures (roads, villages, etc.). However, these factors play a major role in the development of landslides. Thus, this study aims to integrate all these parameters in a holistic analysis of individual landslide events in Rwanda, in order to provide guidelines for hazard assessment.

The Karongi area (Figure 1) was selected for its exceptional cluster of ca. 750 landslides (counting performed in this study based on satellite images) that occurred in a 100 km^2 area over a single night from the 6th to the 7th of May 2018 (Figure 2). This event occurred in a highly populated area and killed 18 persons [38]. This death toll makes the Karongi 2018 event one of the deadliest among the recent landslide episodes. We combined field data, high-resolution satellite images, and climate models to describe the geological, morphological, pedological, and climate context of the landslides in order to understand their triggering factors and dynamics. We demonstrate that the Karongi event was favoured by a 2-month near-continuous rainfall that water-logged the thin soil resting on steep slopes. We suggest that the collapse of the slopes was ultimately triggered by a thunderstorm

(although not so exceptional) that brought rainfall and also wind- and thunder-sourced vibrations, probably leading to thixotropy of the soil, triggering numerous landslides.

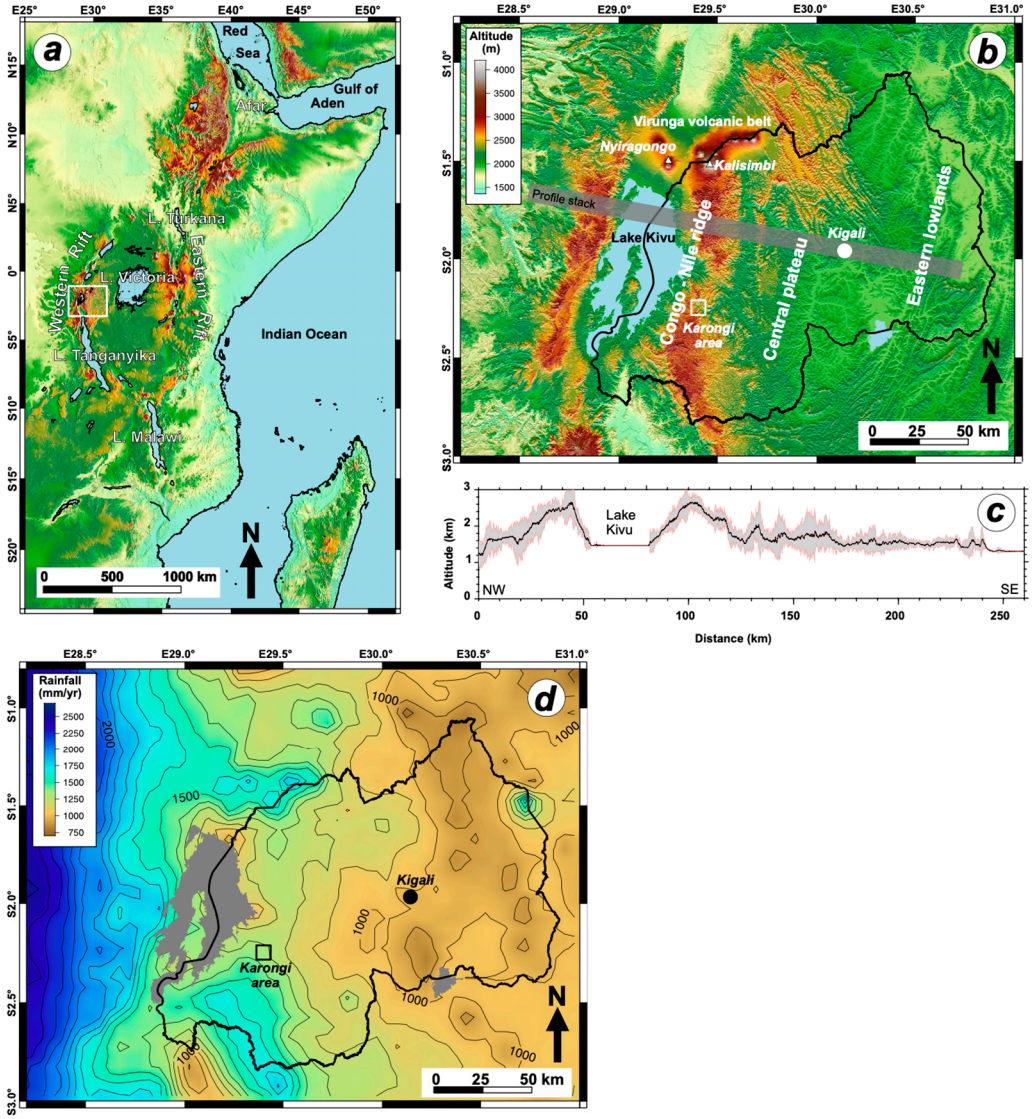

Figure 1. (**a**) Topographic map of Eastern Africa (NASA GTOPO30 DEM) showing the two branches of the rift (the Western Rift and the Eastern Rift) fringing the Lake Victoria high plateau. The white rectangle corresponds to Figure 1b. (**b**) Rwanda elevation map based on the Copernicus 30DEM showing the high topography on both sides of Lake Kivu. The eastern rift shoulder (the Congo–Nile ridge) locally reaches 3000 m in altitude (Figure 1c) and is strongly affected by landslides. The Karongi area discussed in this work is indicated by the white square. The grey rectangle corresponds to the topographic data illustrated in Figure 1c. (**c**) Topographic swap (profiles are sampled every 20 m and separated by 1 km) across the Lake Kivu rift system showing the high altitudes of the Congo–Nile ridge in Rwanda and the progressive eastward flattening towards eastern lowlands of Rwanda and the Lake Victoria plateau. The black line represents the mean value and the grey shaded area indicate the dispersion of the values. (**d**) Mean annual rainfall pattern calculated using CHIRPS [39] annual data from 1981 to 2022. Note the strong contrast between the relatively low rainfall (<1000 mm/yr) in eastern Rwanda and the high rainfall (>2000 mm/yr) in the eastern Congo Basin to the west. Mean rainfall on the Congo–Nile ridge ranges from 1250 to 1500 mm/yr.

Figure 2. Mud–debris flows in the Karongi area. Pictures of the aftermath of landslides that occurred on the 7th of May 2018 [38]. The images are located in Figure 3. Figure 2a is one of the numerous landslides that occurred along the steep Rwankuba crest and Figure 2b corresponds to the "Major landslide" northwest of Burega School. Note that the latest is also labelled on Figure 4.

2. The Study Area: Geologic and Geographic Contexts

The Karongi area is located to the east of Lake Kivu, near the city of Karongi (Kibuye) (Figure 1). The regional geology belongs to the Meso-Proterozoic, strongly deformed tectonic units of the Karagwe Ankolean Belt that characterizes the whole of Rwanda [40]. The lithology is mainly composed of alternating phyllites, quartz-phyllites, and a few quartzitic units (Figure 3). This metamorphic basement is intruded by large Late Proterozoic S-type granitic batholites [40–42]. Since the Miocene, the tectonic activity linked to the opening of the East African Rift has led to the formation of the Kivu graben and the correlated uplift of its shoulders [43,44]. Surprisingly, though the area is seismically active, landslide events in the North Tanganyika–Kivu rift are not correlated with earthquakes [34,37]. In addition, only one significant earthquake of magnitude Mw > 4 has been recorded around the Karongi area in the last 50 years (24 September 2023, Mw = 4.5, depth = 10 km) [45].

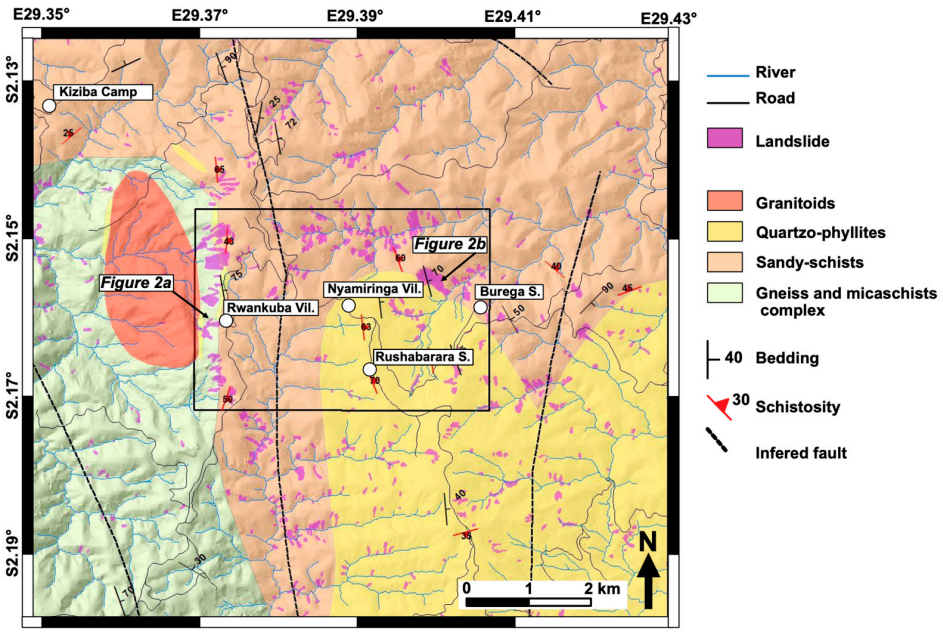

Figure 3. Geological map of the Karongi area adapted from [42,46], incorporating field observations and measurements of lithological and tectonic structures. The black rectangle corresponds to the area studied in more detail in this work.

Because of its location on the Kivu ridge, the Karongi area is mountainous, ranging in altitude between 1600 m and 2700 m above sea level (asl). The landscape is that of a succession of flat-topped hills separated by several 100 m deep steep-sloped valleys (Figure 4). The western part of the study area is limited by the large NNW-SSE Rwankuba ridge, and most of the main valleys trend N-S. The area receives an average annual rainfall of 1300 mm.

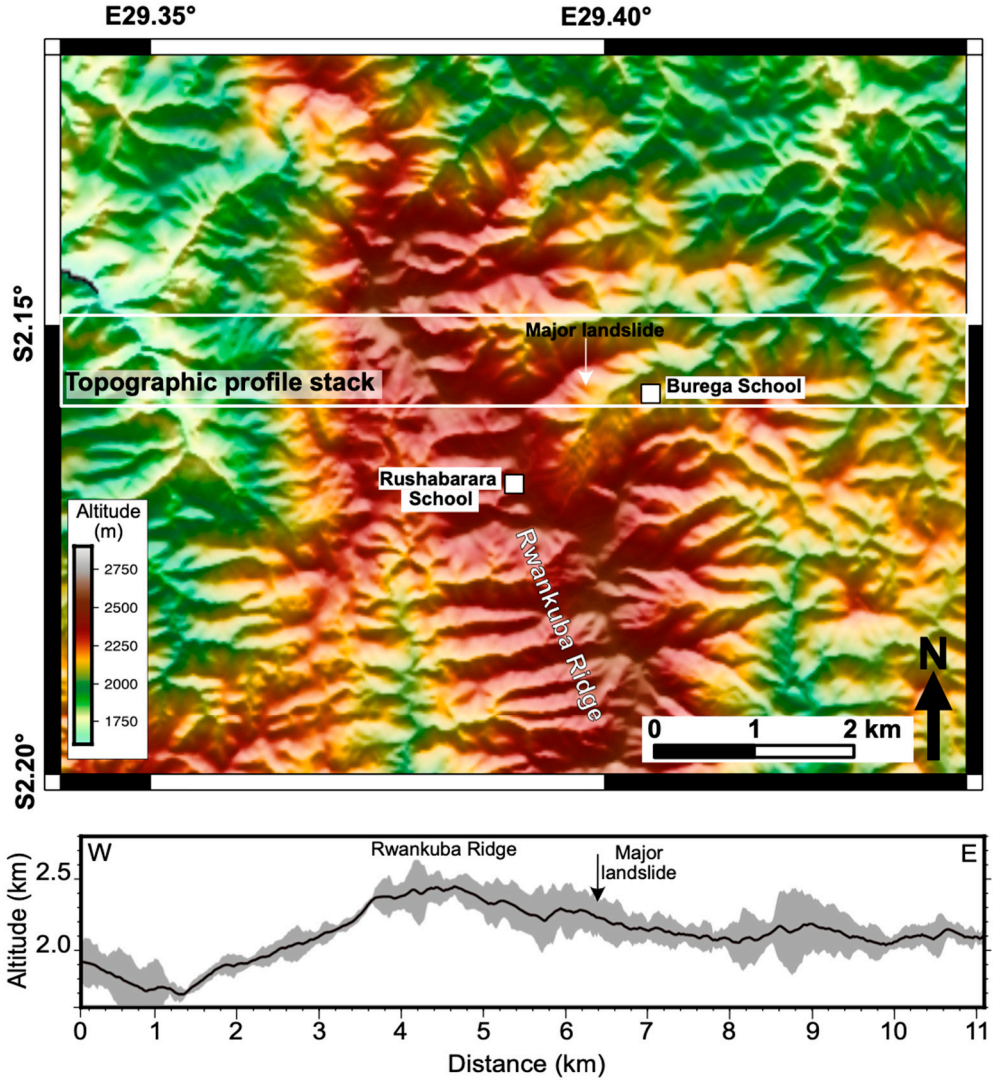

Figure 4. Topography of the Karongi area from COPERNICUS DEM [47]. The topographic profile was constructed by sampling every 20 m along profiles separated by 100 m. The black line indicates the mean topography, while the grey area represents the dispersion of the values. The major landslide indicated is that shown in Figure 2b.

The Karongi region is intensely cultivated, and the land cover is composed of a mix of small forest patches and cultivated fields, some of them arranged into terraces (Figure 5). Forests are composed of very spaced trees, essentially eucalyptus, with very limited undergrowth vegetation. Many of these woods are located on very steep slopes and in places where the humic soil is very thin [48]. The farmed areas include tea plantations, generally cultivated on selected fertile soil, in areas of limited slope. The rest of the farmland is occupied by food crops such as beans, potatoes, bananas, soya beans, and peas, which are interchanged at least twice a year. The Karongi area is densely populated; for example, the Rwankuba sector, where most landslides are located, has a population density of 548.9 pop./km^2 [3] (see location in Figure 5). Houses are made essentially of mud bricks

and generally distributed along gravel roads running on the flat top of mountain ridges. However, a significant number of houses are also built on hill flanks close to cultivated fields, leading to a significant landslide hazard.

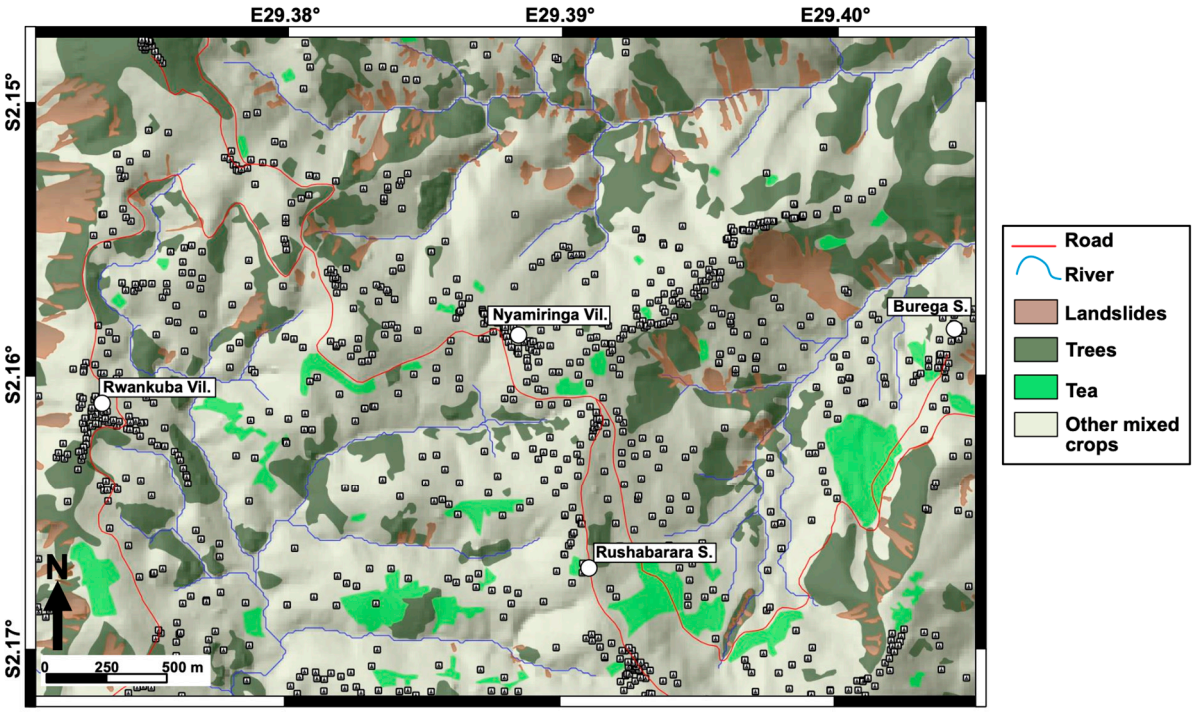

Figure 5. Land use (based on the Google Earth satellite image available for the 1-January-2023) and occurrence of the landslides in the Karongi area based on satellite image analyses.

3. Materials and Methods

The major factors influencing the formation and dynamics of landslides in Rwanda and surrounding regions are steep topography, high rainfall, and the nature and structure of the soil and the consequences of a recent major increase in populations (deforestation, soil degradation, infrastructure building). After conducting an exhaustive inventory of all the landslides corresponding to the 2018 event, we performed a detailed analysis of the geology, geomorphology, soil characteristics, land use, and climate in the Karongi area.

3.1. Landslides Inventory

Landslides were identified from high-resolution optical satellite images (CNES/Airbus) dated from October 2018 and available on Google Earth Pro, which were recognizable from the distinctive shape and colour of the strip and deposition areas (Figure 6). As mentioned above, the Karongi area is covered with fields and patches of forest. Landslides are easily recognizable from their oblong shape and their brownish colour corresponding to soil stripped from vegetation (Figure 6). For the smallest landslides, some confusion with freshly overturned fields may occur, although these generally display a characteristic rectangular shape. Landslides were delineated as polygons to their full extent, including the slide scarp and the spreading zone with deposited material. Fieldwork was conducted in November 2022, April 2023, and November 2023 to describe in detail the landslide morphologies, dynamics of movement, material displaced, underlying bedrock, and soil thickness and structure.

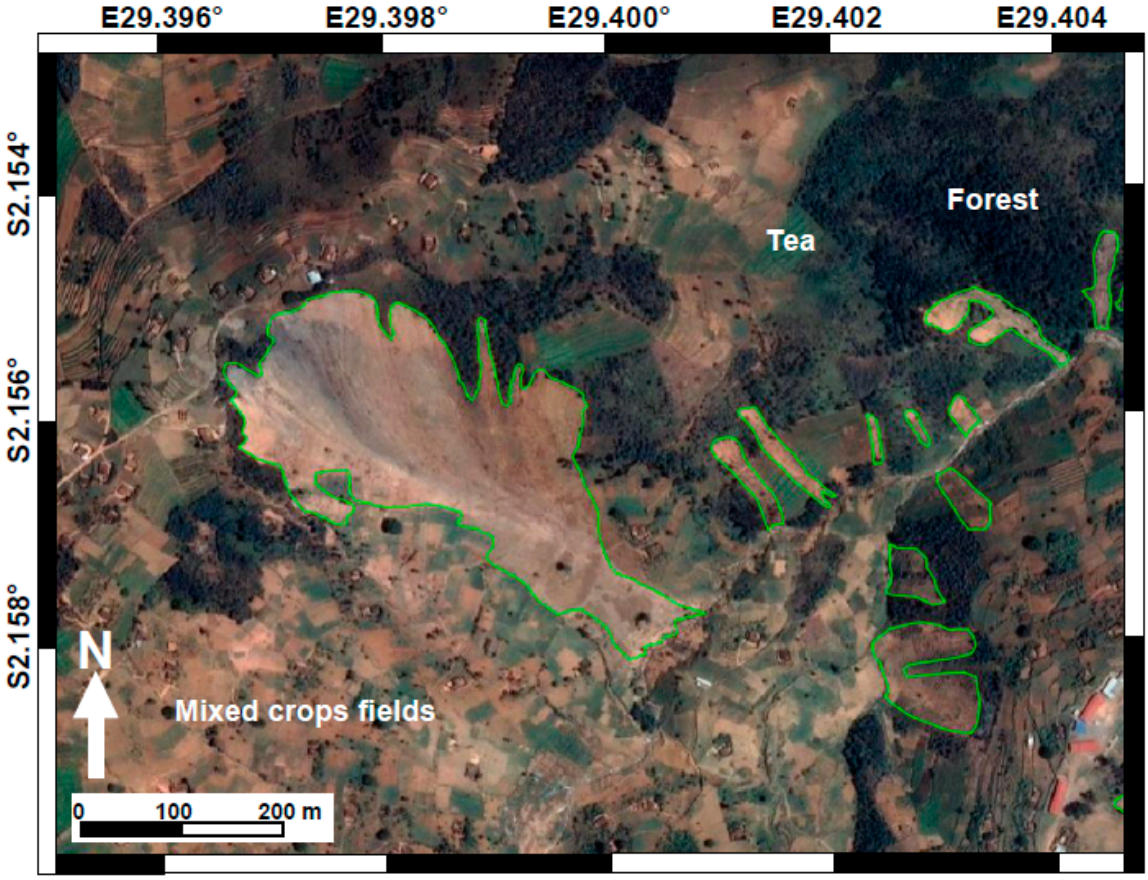

Figure 6. October 2018 high-resolution CNES/Airbus image (via Google Earth) showing the major landslide and adjacent ones (green line contours) in the Karongi area developing on graphitic schists and meta-sandstone bedrock. Outside the landslides, the angular polygons of green and light brown colours are cultivated fields, and the dark green areas are trees (generally eucalyptus). See Figure 2b for an image of the landslide immediately after being triggered.

3.2. Topographic Data

Rwanda has acquired a 10 m resolution Digital Elevation Model (DEM) using stereo-restitution based on 25 cm spatial resolution ortho-rectified aerial images through the cooperation of the Rwanda National Resources Authority (RNRA), the Regional Centre for Mapping of Resources for Development (RCMRD), and the World Bank [49]. This DEM was used in this study to derive slope maps as the slope angle is a primary controlling factor for the occurrence of landslides, especially shallow ones [50]. All other parameters being equal, the probability of landslide occurrence increases with the topographic slope angle. In Rwanda, it has been observed that slopes greater than 25°, especially on phyllitic rocks, are often affected by mass movements and especially by muddy flows [27]. Landslide initiation slopes were calculated from the DEM, using the Raster Zonal Statistics tool available in QGIS software. In every polygon corresponding to landslides, the maximum slope was extracted, and since landslides in Karongi generally have a small area, this value was retained as the initiation slope of the considered landslide. The soil layer affected by landslides is generally thin and parallel to the bedrock (see soil description below); therefore, the slope angles before and after a landslide are very similar and can be considered identical within the error margin of the calculated slope.

3.3. Soil and Substratum Characteristics

Aside from slope, soil characteristics are also important factors in shallow landslide occurrence [51,52]. While the structure and composition of the soil is a key factor in determining landslide susceptibility, soil thickness especially controls the volume and type

of discharge; the thicker the soil, the higher the discharge [53]. Soil characteristics in the Karongi area were assessed in the field at different places where complete soil profiles were exposed (i.e., when both the top humic layer and the basement were observed) either on natural scarps (especially the edges of landslides) or along road and path trenches. Major soil horizons were described to estimate their role in the occurrence of landslides in this area and to constrain the landslide detachment level. The soil thickness data recorded in the field (using a tape measure on exposed complete soil profiles) were interpolated to derive a soil thickness map using Inverse Distance Weighting (IDW) interpolation in QGIS software as follows: georeferenced measured thickness points were weighted during interpolation such that the influence of one point relative to others decreased with the distance from the unknown thickness point [54]. Field measurements of soil thickness were complemented by mapping rock outcrops (corresponding to 0 m soil thickness) on high resolution satellite images (provided by the GoogleEarth platform) in order to increase the accuracy of the interpolated maps. The lithology data obtained from the geological map were complemented by field observations and bedding and schistosity measurements to provide a detailed map of the basement lithology and structure (Figure 3).

3.4. Rainfall and Wind Data

To assess the potential contribution of climatic parameters to landslide initiation, and especially the role of antecedent rainfall [22], we carried out a detailed analysis of the regional rainfall and wind patterns. The rainfall analysis was based on 42 years (1981–2022) of daily rainfall open-access data obtained from the Climate Hazards Group InfraRed Precipitation with Station data (CHIRPS [39]). In the absence of data on the occurrence of previous landslides in the region, calculating an effective antecedent rainfall period [15] was not possible, and we thus focused on determining the specificities of 2018 in terms of rainfall patterns. The CHIRPS data were used to calculate long-term monthly and annual precipitation trends over the whole available period. The Rainfall Anomaly Index (RAI) [55] obtained using the CHIRPS data was used to compute the inter-annual (considering only the March–April period) variability in rainfall within the Karongi area to depict a potential difference between 2018 (year of the Karongi event) and the other 41 years of record in this area. Hourly rainfall, wind speed, and wind direction data from the European Centre for Medium-Range Weather Forecasts ERA5-Land reanalysis model [56] were used to locate and characterize rainstorm events within the month preceding the landslide event on the 7th of May 2018. Thunderstorms were mapped using both the rainfall and wind data, i.e., a thunderstorm corresponds to a combination of localized heavy rain and locally strong, centripetal winds (note that ERA5-Land only provides the horizontal wind component, although the vertical component can be high in such convective cells).

4. Results

4.1. Geology and Soil Structure in the Karongi Area

The lithology and structure of the geological basement can play a major role in the development of landslides. Lithology can participate in controlling the type, thickness, and structure of the overlying soil ([57] and references therein). Structures like bedding planes, fractures, or schistosity can affect the mechanical behaviour, facilitating ruptures when interacting with topographic slopes [58] or allowing for larger rainwater infiltration rates.

The metamorphic basement of the Karongi area is composed of various units of different lithologies [42]. In general, bedding trends NNW-SSE with dip angles varying from 25 to 75° (Figure 3). Schistosity is largely near parallel to the bedding except in a few strongly folded areas. Several N-S trending faults are reported on the geological map [42,46], for which age is underdetermined. However, although strongly altered zones secant to the bedding and schistosity that could represent shear zones are observed in the series, surface weathering makes it impossible to identify fault kinematics. To the north and on a ca. 1 km wide N-S strip east of the main Rwankuba ridge, the lithology is dominated by meta-sandstones inter-layered with schists, some of them graphitic. The Rwankuba

ridge itself is armoured by a series of metre-to-decametre-thick meta-sandstone layers dipping some 50 to 60° eastward and forming a 60 to 70° steep cliff to the west. To the SW, the basement is composed of gneisses and micaschists intruded by a small granitoid pluton. Finally, to the SE of the study area, the basement is formed by phyllites inter-layered with quartzites.

The humid equatorial climate of Rwanda makes for strong soil weathering. Following a long Mesozoic and Cenozoic history of regional-scale surface planation and alteration [59–61], some several-metres-thick alteritic profiles formed during the Plio-Quaternary before being partially or completely reworked because of the topographic changes induced by the tectonic activity in the East African Rift system [62,63]. Outside of the landslide deposition areas, the measured soil thickness varies between 0 m and 3 m, mainly depending on the local slope (Figure 7). The maximum thickness values are found in the river valleys where fluvial and diffusion accumulation occur, while in most of the area, the soil thickness varies between 0.5 and 2 m. The soil structure seems to be the most complete on the flat-topped ridges; Figure 8 shows the following:

- The O horizon (litter layer) is very limited (0 to a few centimetres in thickness), except in wooded areas where it is formed by leaf accumulation.
- The A horizon (humic topsoil) is generally restricted to a few centimetres to decimetres, except in some very specific areas on top of the ridges where it can reach up to 1 m.
- The E and B horizons (leaching layer and subsoil) are difficult to distinguish and generally form a near-homogeneous layer. When developed on meta-sandstones and schists, it is composed of a reddish to light brown mixture of sand and clay, 0.5 to 2 m thick. A few dispersed pebbles and blocks of basement rocks are frequently observed within these horizons. In places where the substratum is formed by graphitic schists, this E + B horizon is mainly composed of brown clay.
- The C horizon (weathered parent material) is represented by a centimetre- to decimetre-thick layer of clasts, ranging in size from gravels to blocks, moderately rounded to angular. Those clasts are mainly quartzite and locally derived meta-sandstones. Some of them show iron coating, suggesting the existence of a strong lateritic phase, although no evidence of iron crust has been observed.
- Depending on its dominant lithology, the R horizon (parent material) can be strongly weathered, especially when composed of graphitic schists.

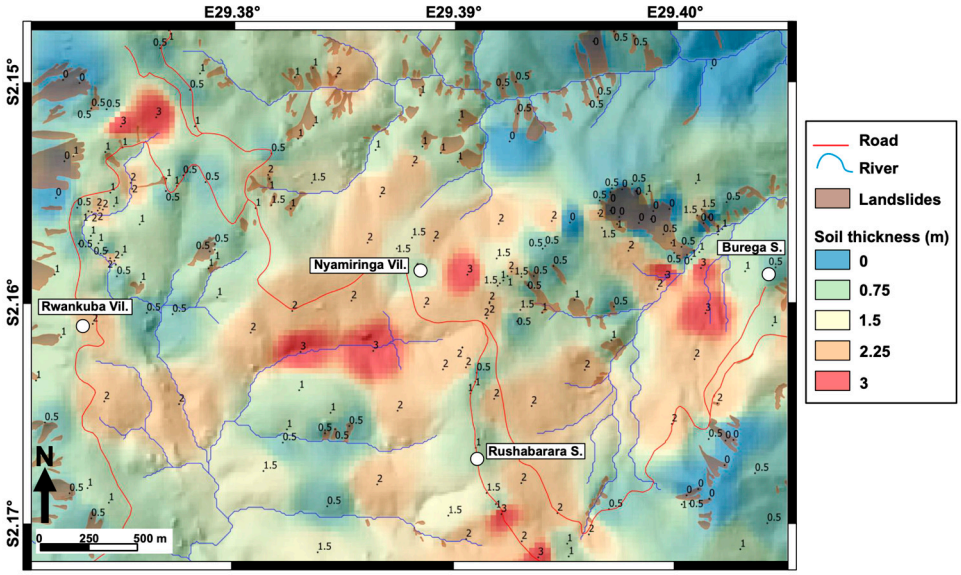

Figure 7. Interpolated map of soil thickness in the Karongi area created by the Inverse Distance Weighted (IDW) method. Black dots and associated numbers show the location of the data points and their associated soil thicknesses (rounded to the upper 0.5 m value). As indicated in Section 3.3, thickness was measured on exposed complete soil profiles using a tape measure.

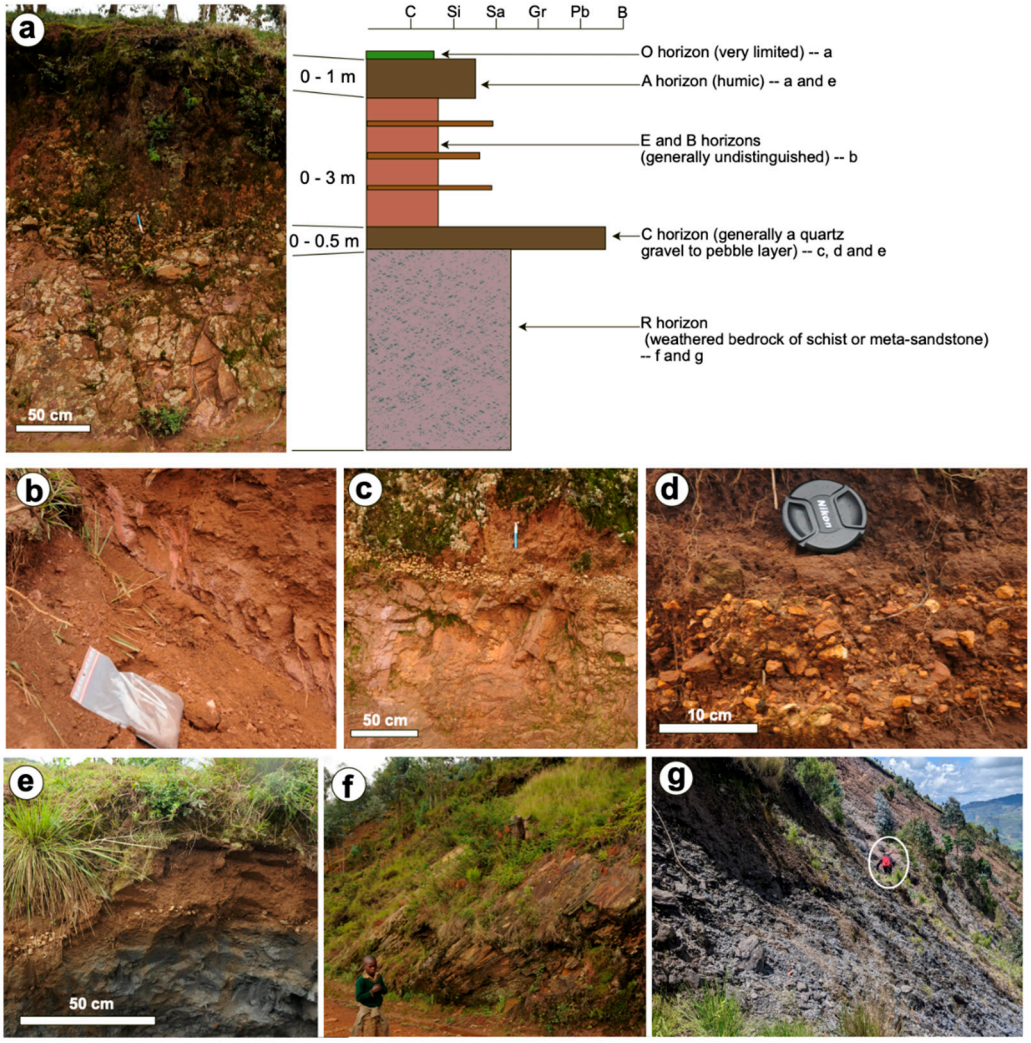

Figure 8. Main soil characteristics of the Karongi area. (**a**)—General view of a soil profile and corresponding idealized section indicating the different horizons with their range of thicknesses. The letters a to g are related to the pictures. (**b**)—Undifferentiated E and B horizons developing from a bedrock composed of meta-sandstone. (**c**)—Large-scale view of the quartz gravel layer forming the C horizon on meta-sandstone bedrock. (**d**)—Close view of the C horizon. Note that the quartz gravels and pebbles are poorly rounded. (**e**)—Soil profile developing on graphitic schist bedrock. (**f**)—Large-scale view of the soil-barren meta-sandstone/quartzite basement (R horizon). (**g**)—Large-scale view of the soil-barren graphitic schist bedrock (R horizon).

When present, the soil resting on steep slopes is very thin (generally less than 1 m), although still structured the same way as on the top of the hills (Figure 9). Finally, the soil occupying the bottom of the flattest valleys is more heterogeneous, formed by colluvium and/or, in some cases, fine-grained deposits marking ephemeral lakes or swamps created by damming from landslides.

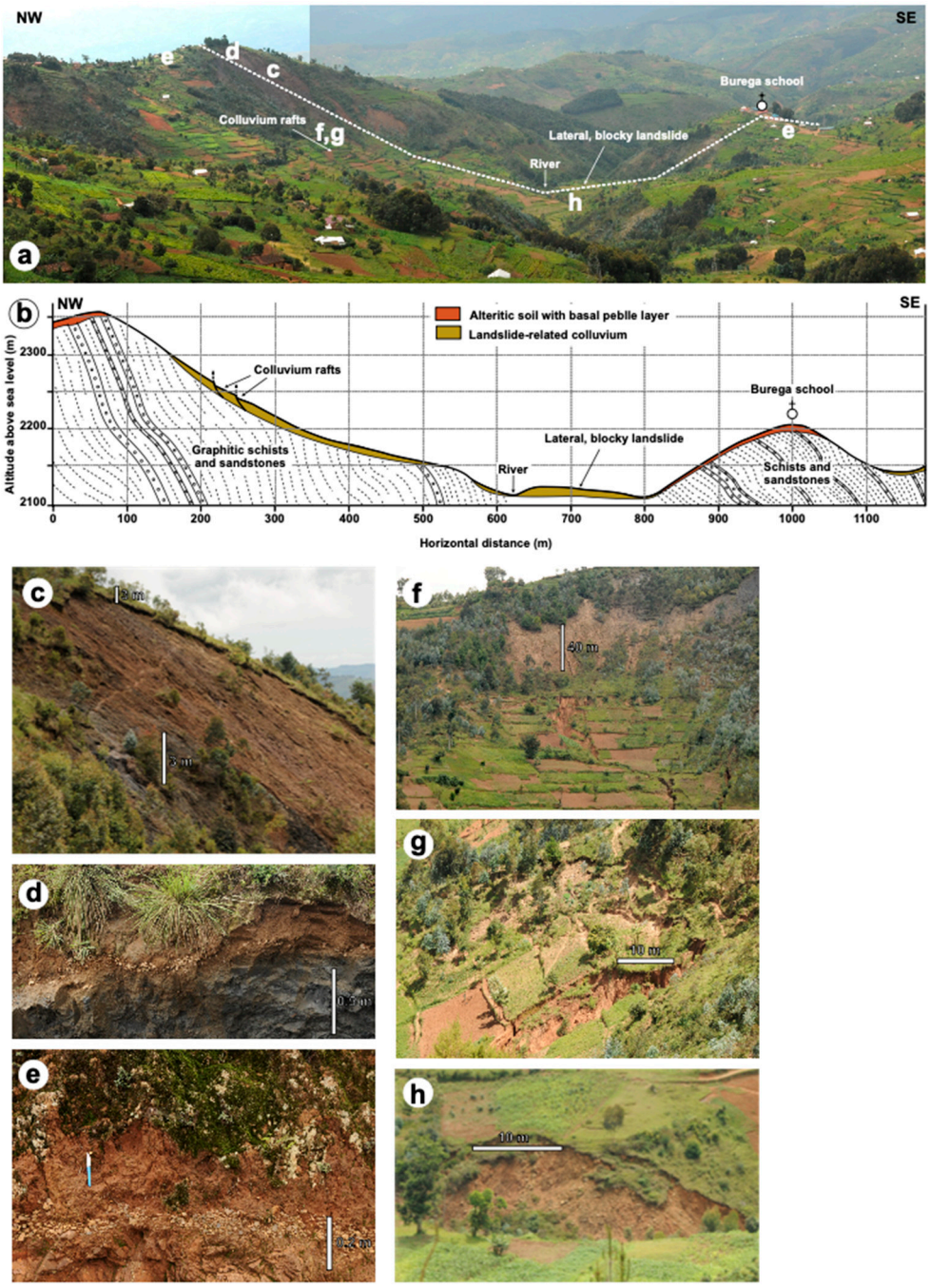

Figure 9. Landscape (**a**) and cross-section (**b**) of the main landslide in the Karongi area (see Figure 6 for localization). The pictures illustrate the main elements and are reported in the section and general picture. (**c**)—Detachment zone of the landslide in the graphitic schists. Note the very steep slope (about 60°). The surface is covered with pebbles and blocks of schists from the underlying basement. (**d**)—Soil section at the top of the landslide showing dark strongly weathered graphitic schists (R horizon) overlaid by a thin layer of quartz pebbles (C horizon) that separate the R horizon from a very condensed E, B, and A horizon stack. (**e**)—Similar soil profile but developed in non-graphitic schists and sandstones. (**f**)—Lower part of the detachment zone: the break in topographic slope is sharp, and a large amount of colluvial material is deposited in that area, affected by open cracks. (**g**)—The thick colluvial layer collapsing downslope as metre-thick coherent rafts of clay–sandy material with few blocks. (**h**)—Blocky material of an older landslide that occurred on the SE slope of the system in a sandstone-rich basement unit. Note that for the landscape pictures (**c**,**f**–**h**), the scale varies with distance.

4.2. Landslide Morphologies

Landslides in the studied area are generally of small area, ranging from 50 m^2 to 68,000 m^2, with a median surface of 1850 m^2 (including striped areas and downslope deposits). According to the updated Varnes classification [64,65], the observed May 2018 Karongi landslides were shallow mud–debris slides (avalanches and flows). As shown in Figure 2, the material is very liquid, indicating a high water content, and is deposited as a thin sheet of mud preserving the topography of the cultivated terraces. The median angle of the topographic slope for landslide initiation in May 2018 was 40°, with maximum slopes reaching 60° (Figure 10). Few landslides (about 3%) occurred on shallow slopes between 20 and 30°, probably favoured by the low viscosity of the material. Where observed, the detachment zone is always situated between the pebbly layer forming the C horizon and the underlying bedrock (Figures 8 and 9).

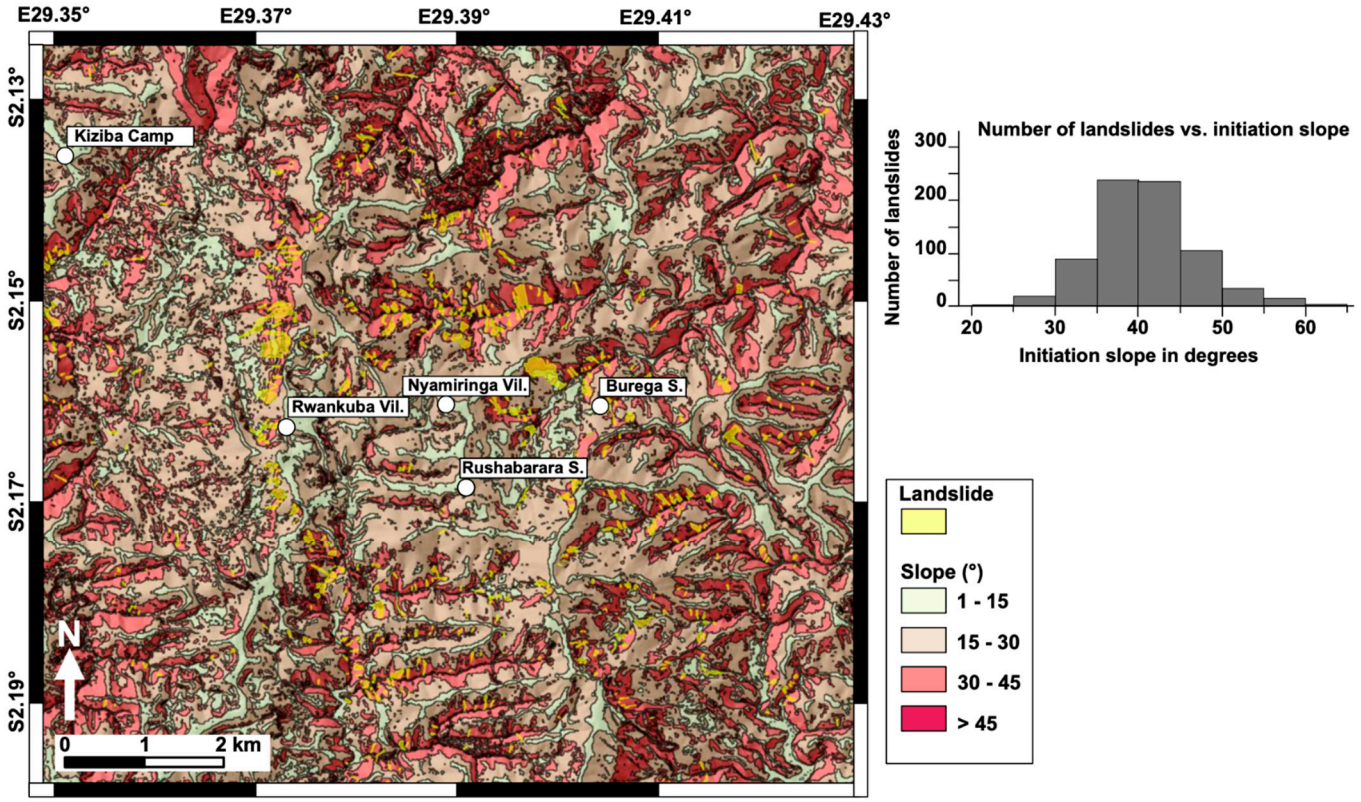

Figure 10. Slope map of the Karongi area with the position of the landslides (yellow polygons). The histogram represents the density of landslides versus the landslide initiation angle.

The largest landslide, which occurred on the northern flank of the Nyamiringa River valley (see location in Figure 4 and refer to Figures 6 and 9 for morphological characteristics), provides a good example of the morphology and kinematics of the Karongi landslides. Based on the images and the description made by local people, the landslide occurred as a low-viscosity mudflow that covered the landscape with a thin (< 1 m thick) sheet of mud and few larger elements of pebble to small blocks size made of locally derived basement lithologies (Figure 2). The landslide was triggered on a steep slope, locally > 50° developed on graphitic schists with schistosity dipping about 70°, near parallel to the slope (Figure 9). The top of the hill is capped by the 1 to 2 m thick characteristics of the soil described above. The surface of the striped area is covered with angular pebbles and small blocks of the underlying graphitic schists (corresponding to the C horizon described above), indicating that the material was mobilized above that layer (Figure 9c,d,e). Downslope, at the foot of the steepest slope, reddish, poorly sorted, sandy colluvium including floating blocks of local basement reach up to 3 m in thickness. These colluviums are affected by

internal shear zones limiting rafts of material sliding down the slope and creating open cracks perpendicular to the slope (Figure 9f,g). Lower down, the deposits are progressively thinner, reaching about 1 m in the lowermost deposition area. The material is still poorly sorted but the matrix is much finer-grained (mostly fine sand, silt, and clay) and the proportion of blocks tends to increase. Those deposits are incised by narrow, regressive gullies (several metres deep in the upper part), some of them reaching the basement rock on the steepest slopes. The Nyamiringa River flows at the foot of the landslide, incising the basement rock and creating about a 5 m high knickpoint immediately downstream of the landslide. To the south of the river, ca. 10 m high terrace is composed of poorly sorted blocky material that we attribute to an old, large landslide that originated from the southern slopes of the valley, which probably blocked the Nyamiringa River creating a temporary dam (Figure 9h). Indeed, upstream of that gravity deposit, the valley floor is flat, filled with fine-grained material most probably deposited in an ephemeral dam–lake environment. Finally, the north-facing slope of the hill supporting the Burega school (Figures 6 and 9) is again covered by a 1 to 2 m thick reddish soil characteristics of the area, deposited on phyllites with alternating quartzites. This slope was also affected by small landslides in 2018.

4.3. Long-Term Climate and Extreme Weather Conditions in Spring 2018

Based on CHIRPS data, the total yearly precipitation oscillated between 950 mm and 1600 mm, with an average of 1300 mm during the 42 years of the record (1981–2022) (Figure 11a). The rainiest year was 1987 (1525 mm), while the driest was 2008 (963 mm). The year of interest in this study, i.e., 2018 (1428 mm), was the fifth rainiest year (Figure 11a). The so-called ''long rainy season'' (a period covering March to May) received the most precipitation (Figure 11b), but, practically, it rained abundantly during nine consecutive months from September to May (rainfall > 100 mm/month). The dry season extended from June to August (Figure 11b). March 2018 (229 mm) and April 2018 (233 mm) received a considerable excess of precipitation compared with the long-term average monthly rainfall of 156 mm (March) and 161 mm (April), summing to a total precipitation excess of 143 mm in the two months that preceded the landslide event. This is also shown by an outstanding RAI value (>5) (Figure 11c) for March–April 2018 compared with those of the other 41 years: the period March–April 2018 was the most humid in 42 years in the Karongi area. Previously, only 2013 (256 mm) and 1999 (240 mm) had a rainier March than 2018, and 1985 (275 mm) and 1986 (246 mm) had a rainier April. Only 1985 reached a combined March–April rainfall level (423 mm) close to that of 2018 (462 mm), although it was still lower.

Rainfall in the Karongi area was near-continuous in the period preceding the 7th of May 2018, with a total of 42 rainy days from the 1st of March to the 6th of May (a day is considered rainy when CHIRPS precipitation values exceed 1 mm), i.e., 3 days over 5 days in average. This was the highest number of rainy days during that period over the 42-year record (Figure 11d). The two days (the 5th and 6th of May) preceding the landslide event were the rainiest consecutive days in that period, with a total rainfall amount of 57.6 mm (Figure 11e).

Heavy rain events such as thunderstorms are prone to trigger landslides; indeed, local inhabitants indicated that the Karongi event occurred simultaneously with an impressive thunderstorm. However, as usual with oral reports, the appreciation of the strength of that storm, especially in terms of rainfall intensity, varied widely from nearly no to exceptionally heavy rain. These storms are poorly resolved in the daily CHIRPS data. Although the ERA5 and ERA5-Land models are known to misestimate the absolute rainfall amount associated with storms in tropical regions [66–69], their hourly resolution still allows for detecting and localizing them. The ERA5-Land data were used to determine the number, position, and relative strength of rainstorms in the Karongi region during the period from the 1st of March to the 6th of May 2018. (Figure 12). Five events combining high rainfall and strong wind were detected over the considered period (Figure 12c). Other days such as the

26th of April recorded high rainfall but no wind or inversely, such as the 7th of April, and are not considered thunderstorms. It is to be noted that the last event on the 6th of May displayed a low rainfall amount and a medium windspeed value relative to the others. The strongest event was recorded on the 11th of April, nearly one month before the Karongi landslide event.

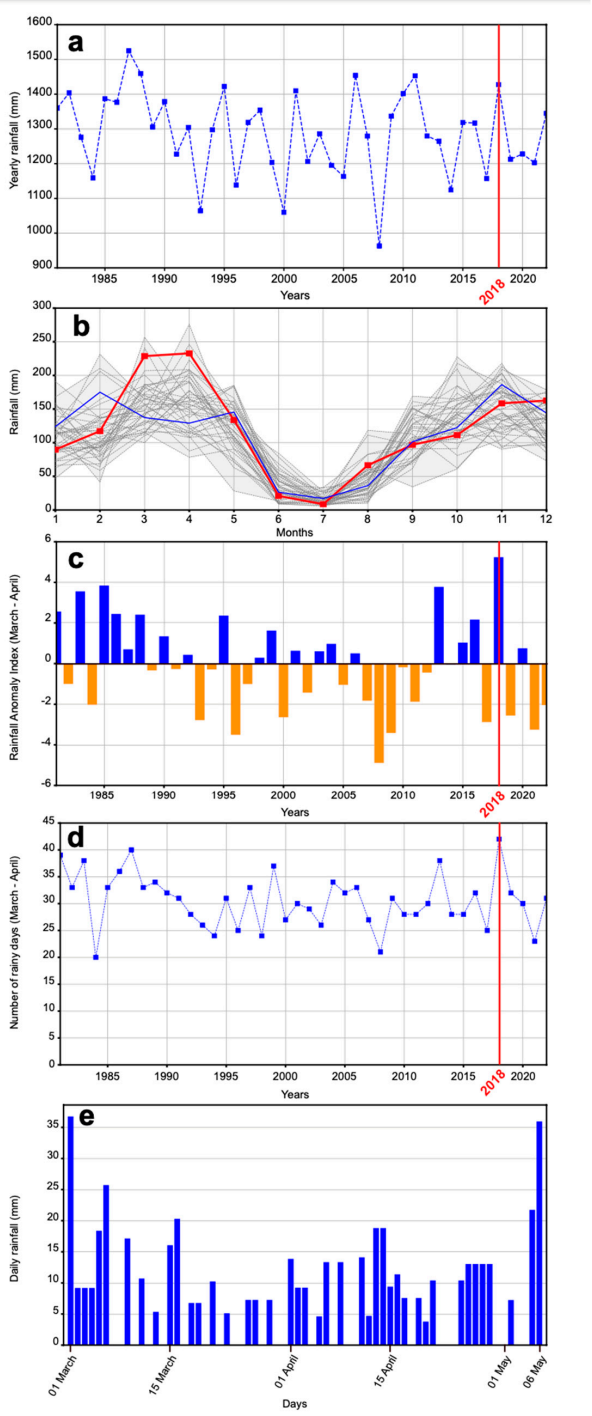

Figure 11. Rainfall in the Karongi area calculated from CHIRPS data. (**a**): Yearly rainfall from 1981 to 2022. The red line indicates 2018. (**b**): Monthly rainfall over the 42 years. The grey envelope includes the dispersion of the data. The blue line is the mean value for each month. The red line corresponds to 2018. (**c**): Calculated March–April Rainfall Anomaly Index (RAI) for the period 1981–2022. (**d**): Total number of rainy days in March–April over the 42 years. The red line indicates 2018. (**e**): Daily rainfall from 1 March to 6 May 2018.

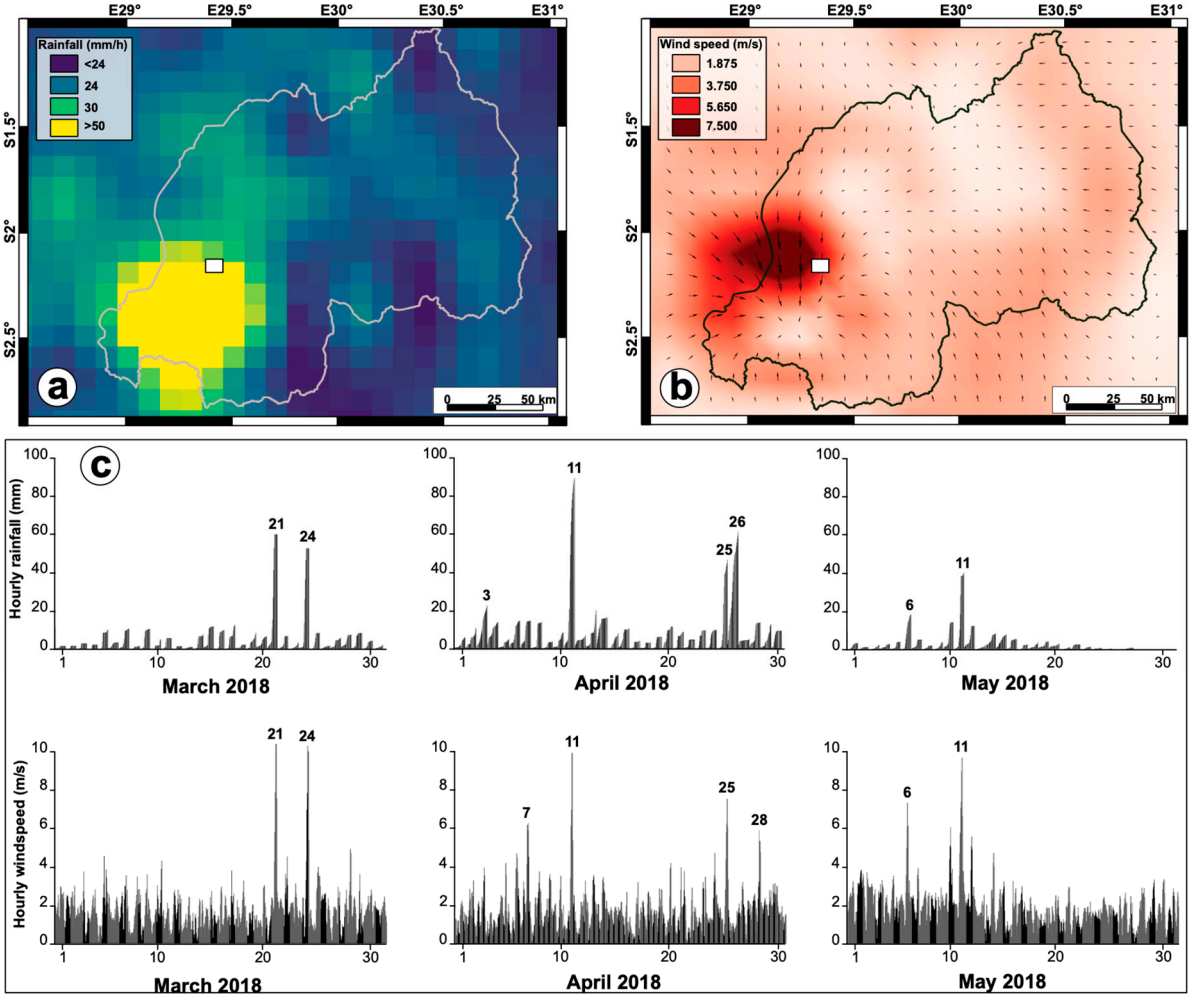

Figure 12. Detection of stormy events in the Karongi area (white rectangle on Figure 12a,b refers to the area covered by the geomorphology study) using the ERA5-Land reanalysis data. (**a**) Example of an hourly precipitation map showing a major storm cell positioned in SW Rwanda (the grey line indicates the border of the country). (**b**) Wind speed (red colours) and direction (black arrows) associated with the same cell. (**c**) Hourly precipitation (top) and windspeed (bottom) between the 1st of March and the 6th of May 2018. Numbers indicate the day of major events. Events including both exceptional rain and wind are considered to represent storms.

5. Discussion

Individual landslides occur through a conjunction of slope instability and an external triggering event such as heavy rainfall, soil defrosting, or earthquakes. However, except when related to major rainfall events [70] or a strong earthquake [71,72], the formation of massive landslide clusters over relatively large areas such as in Karongi remains poorly documented and understood [25]. Based on the data presented above, we discuss the parameters that led to the simultaneous triggering of about 740 landslides of all sizes reported in our study area.

Heavy rainfall during the rainy seasons, especially in April and May, is the most commonly accepted landslide-triggering mechanism in Rwanda. However, our results suggest a more complex mechanism at the origin of the Karongi cluster. The analysis of the CHIRPS data indicates that March and April 2018 were not only exceptional in terms of the total amount of precipitation but also in terms of the number of rainy days (Figure 11). The soil structure in the Karongi area is mainly characterized by a low-permeability, clay-rich layer including the E and B horizons, resting on a C horizon composed essentially of a layer of gravel to blocks (Figure 8). This coarse horizon represents both a layer of low shear stress

and a layer of water storage. Associated with the steep slopes of the Karongi region, this makes for very unstable soil cover that is prone to developing shallow landslides [73,74]. The high population density leads to intensive exploitation of land using non-mechanized processes. Except for the growing number of tea plots, crops on individual plots are rotated at least three times a year, even on the steep slopes. Soil overturning down to 50 cm or so increases the soil permeability by creating a fragmented surface (from overturning) and reducing the vegetation cover. The increased rainfall infiltration and the absence of a permanent root system (or its very limited efficiency in the areas covered with eucalyptus) reduces the soil stability [75–77].

Coulomb-type materials are a biphasic mixture of grains and fluid in which, following the Mohr–Coulomb theory, shear stress depends on the normal constrain τ_N. This constrain, which affects both the interstitial fluid and the contacts between the grains, can be formalized as follows:

$$\tau_N = \tau'_N + p \quad (1)$$

where p is the interstitial pressure and τ'_N is the normal effective constrain [78]. The onset of sliding occurs when the flowing-threshold constrain τ_C is reached:

$$\tau_C = C + \tau'_N \tan(\varphi) \quad (2)$$

where φ is the internal frictional angle and C is the cohesion of the material.

Mudflows such as those characterizing the landslides in the Karongi district result from rapid liquefaction of clay-rich material following thixotropic behaviour [79–82]. When the thixotropic material initiates movement under a stress higher than the maximal equilibrium shear stress (i.e., $\tau_N > \tau_C$), its viscosity decreases sharply, leading to liquefaction. As shown in Figure 2, the mudflows in Karongi were extremely fluid and largely saturated with water. We suggest that the near-permanent, exceptionally high precipitation of March–April 2018, associated to the agriculture-related increase in infiltration, saturated the soil (Figure 13a). This increased the interstitial fluid pressure (p), thus reducing the normal effective constrain (τ'_N) following Equation (1), and reduced the cohesion [83], which in turn lowered the flowing-threshold constrain τ_C (Equation (2)). Because the porosity of the gravelly C horizon is higher, the fluid pressure in that layer (p_2) especially increased compared with that in the less porous clay-rich soil (p_1).

However, an external mechanism is needed in order for several hundreds of landslides to be triggered simultaneously on slopes with locally varying soil thicknesses, internal structures, and compositions. Aside from heavy rain, ground shaking from earthquakes is another major mechanism that triggers landslides [71,72]. However, no earthquake was recorded in the Karongi region or even in western Rwanda in late April or early May 2018. The analysis of the climatic conditions from ERA5-Land data highlighted a series of five thunderstorms between early March and the 6th of May, the latest being simultaneous with the landslide event, although not the largest (Figure 12). Soil vibration from the strong winds and the sound waves linked to thunder may be at the origin of the thixotropic liquefaction of the water–saturated soil. Small vibrations such as sound waves applied to a granular material induce a re-organization of the grains that leads to compaction [82,84] and, in a non-confined material, also allows for the activation of flow [85]. The characteristics of thunder-generated acoustic waves in the seismic record have long been recognized [86–88], and some studies suggested they could be used to describe the near-surface (down to several metres) ground velocity structure [89]. Measured vertical ground motion linked to thunderstorms is of the order of 0.1 to 2 microns/s and amplifies down from the surface while the radial peak-to-peak amplitudes decrease rapidly [88]. Similarly, wind energy is the source for a number of seismic signals including both horizontal and vertical motions [90,91]. Such signals are recordable down to ground depths of several 10 to 100 m [92]. In particular, seismic waves generated by the interaction of surface obstacles like trees are known to generate ground motions similar to or higher than small *M* 1.0–1.5 earthquakes [92–94]. Depending on the wind speed and the nature of

the obstacles (including the nature of the connexion with the ground), recorded vertical movement can reach 10 microns/s [92].

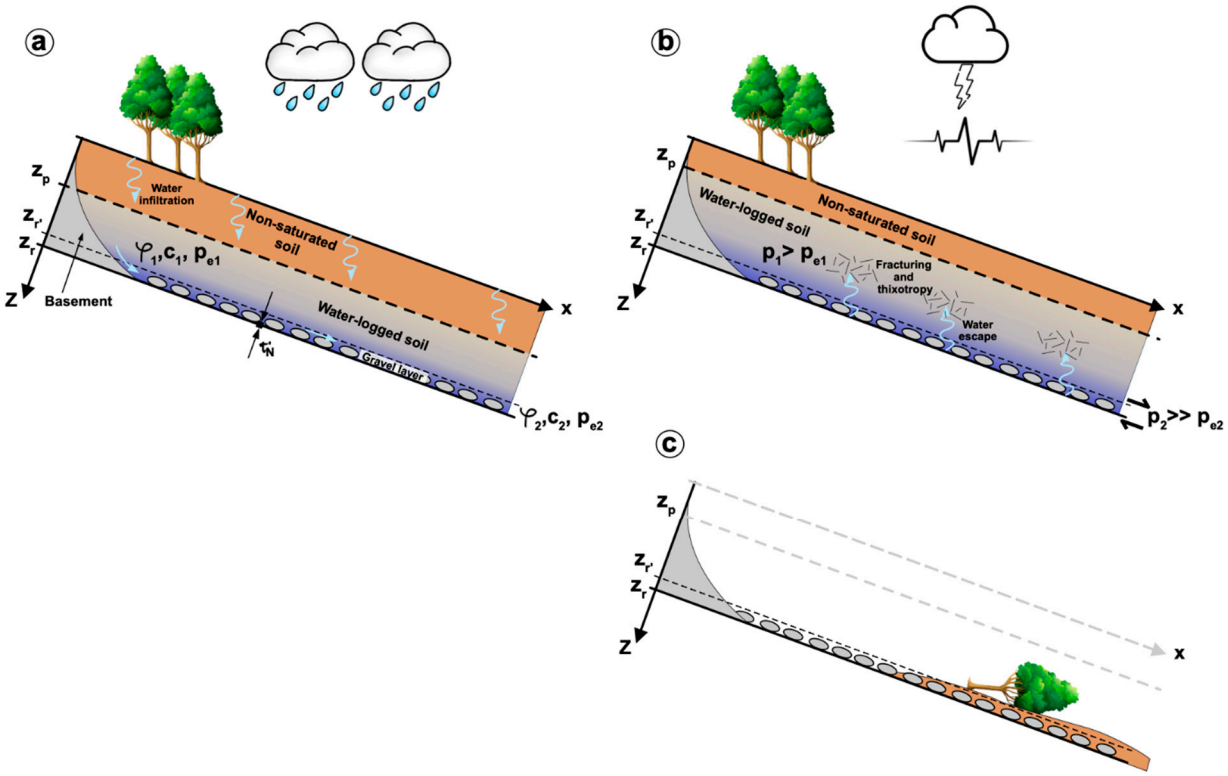

Figure 13. Proposed model for the formation of the Karongi landslides. (**a**) The soil rests at equilibrium on the slope, limited from the basement by the gravel layer of the C horizon (note that for better representation, the thickness of the C layer as well as the size of the pebbles is over-exaggerated. φ_1, C_1, p_{e1}, and φ_2, C_2, p_{e2} are the internal frictional angle, cohesion, and interstitial pressure, respectively, in the clay-rich soil and gravely C horizon. q is the surface slope angle, Z_p is the water table level, Z_r and $Z_{r'}$ are the limits of the rupture layer, and τ'_N is the normal effective constrain. The light blue arrows indicate water infiltration from the surface and preferential circulation within the C horizon. The brown layer represents the non-saturated part of the E + B horizon, and the blueish layer represents the progressively saturated part of that horizon with a higher water content at the base and in the C horizon. (**b**) Because of continuous rainfall, the water table level rises with time. When saturation reaches a near threshold, vibrations linked to sound waves during a thunderstorm event induce a rise in the interstitial fluid pressure p_1 and especially p_2 that become larger than the respective equilibrium pressures p_{e1} and p_{e2}, initiating soil movement and triggering thixotropy in the clay-rich layer. (**c**) Final situation after the landslide.

The detailed parameters involved in the physical mechanisms leading to this exceptional landslide cluster remain to be determined. However, based on the data presented above, we propose that while the thunderstorms that preceded that of the 6th of May appeared generally stronger in terms of rainfall and wind speed, they occurred prior to the complete water saturation of the soil, and especially of the C horizon, where the fluid pressure remained below the equilibrium pressure (p_{e2}). Between the 25th of April and the 6th of May, the saturation reached a threshold that, under the mechanical solicitation of the sound waves and/or wind-induced vibrations, increased fluid pressure in both the C horizon and the water-logged, clay-rich soil above (Figure 13b), decreasing the cohesion (C) of the material and triggering the initial movement. Since clay-rich soil has a thixotropic behaviour, this movement initiated liquefaction and the catastrophic landslide (Figure 13c).

Individual mudflows of the same type as the Karongi landslides are frequently observed in western Rwanda, and their detailed analysis, similar to the one reported here,

should help validate the proposed model, especially the mechanism leading to the initial thixotropic behaviour. Indeed, aside from natural acoustic or mechanical waves (wind, thunder, earthquakes), man-made tremors such as mine or road construction blasting may also be an initiation factor. In terms of hazard warning, an effort should also be made to recognize (and forecasting) the periods of peculiar rainfall conditions leading to progressive soil water-logging, especially in regions of thin, layered, clay-rich soils.

6. Conclusions

The cluster of ca. 750 simultaneous landslides that occurred in the Karongi district in May 2018 resulted from a combination of an exceptionally rainy two-month period before the event, a peculiar soil structure characterized by a coarse-grained C horizon allowing water storage, steep slopes, and a thunderstorm as the ultimate triggering mechanism. The proposed model remains to be further tested. Indeed, the detailed physical mechanisms underlying the proposed model should be further investigated, especially by determining the exact soil properties (cohesion, porosity, etc.) required to perform numerical stability tests. Understanding the parameters leading to the Karongi event is the first step toward prevention. Indeed, while heavy rain is usually accepted as the forcing parameter for landslides, the Karongi landslides are not linked to exceptionally heavy rainfall but to the progressive water saturation of the soil and the sudden triggering of thixotropy by acoustic waves during a thunderstorm. In this case, a hazard warning should have derived from the recognition of the medium-term (two-month) weather pattern rather than from the forecasting of a particularly strong storm. Nonetheless, this study highlights the necessity of a better assessment of the soil properties in the hilly region of Western Rwanda and comprehensive monitoring of the local weather conditions.

Author Contributions: Conceptualization and supervision: M.J., O.D., and D.A.; material preparation, data collection, and analysis: F.-V.B., M.J., O.D., and D.A.; writing—original draft: F.-V.B. and M.J.; writing—review and editing: F.-V.B., M.J., O.D., D.A., and C.H.N. All authors have read and agreed to the published version of the manuscript.

Funding: This work was funded by the Centre National de la Recherche Scientifique 80PRIME MITI program and The University Rennes International Collaboration program.

Data Availability Statement: The datasets generated and analysed during this work are either publicly available on websites referenced in the text (CHIRPS and ERA5-Land climate data, Copernicus DEM) or available upon reasonable request to the authors.

Acknowledgments: The authors would like to thank the Centre National de la Recherche Scientifique–Institut National des Sciences de l'Univers (CNRS–INSU) for support and S. Guillot (CNRS–INSU) for initially promoting this project. This project was carried out as part of a scientific collaboration between the Ministry in Charge of Emergency Management of Rwanda (MINEMA) and the University Rennes. Finally, we would like to thank the three anonymous for their helpful comments on the first versions of this manuscript.

Conflicts of Interest: The authors declare no conflicts of interest.

References

1. Wisner, B.; Blaikie, P.; Cannon, T.; Davis, I. *At Risk: Natural Hazards, People's Vulnerability and Disasters*, 2nd ed.; Routledge: London, UK, 2003; ISBN 978-0-415-25216-4.
2. Kervyn, M.; Jacobs, L.; Maes, J.; Bih Che, V.; de Hontheim, A.; Dewitte, O.; Isabirye, M.; Sekajugo, J.; Kabaseke, C.; Poesen, J.; et al. Landslide Resilience in Equatorial Africa: Moving beyond Problem Identification! *Belg. Rev. Belg. Géogr.* **2015**, *1*, 1–22. [CrossRef]
3. National Institute of Statistics of Rwanda. *Fifth Rwanda Population and Housing Census, 2022 Main Indicators Report*; National Institute of Statistics of Rwanda: Kigali, Rwanda, 2023; pp. 1–150.
4. Delvaux, D.; Mulumba, J.-L.; Sebagenzi, M.N.S.; Bondo, S.F.; Kervyn, F.; Havenith, H.-B. Seismic Hazard Assessment of the Kivu Rift Segment Based on a New Seismotectonic Zonation Model (Western Branch, East African Rift System). *J. Afr. Earth Sci.* **2017**, *134*, 831–855. [CrossRef]
5. Pouclet, A.; Bellon, H.; Bram, K. The Cenozoic Volcanism in the Kivu Rift: Assessment of the Tectonic Setting, Geochemistry, and Geochronology of the Volcanic Activity in the South-Kivu and Virunga Regions. *J. Afr. Earth Sci.* **2016**, *121*, 219–246. [CrossRef]
6. Moeyersons, J. Recherche Géomorphologique Rwanda. *Bull. Soc. Géogr. Liège* **1991**, *27*, 49–68.

7. Ntwali, D.; Ogwang, B.A.; Ongoma, V. The Impacts of Topography on Spatial and Temporal Rainfall Distribution over Rwanda Based on WRF Model. *Atmos. Clim. Sci.* **2016**, *6*, 145–157. [CrossRef]
8. Rwanda Environment Management Authority. *Rwanda State of Environment and Outlook Report*; Rwanda Environment Management Authority: Kigali, Rwanda, 2009; pp. 1–177.
9. Depicker, A.; Govers, G.; Jacobs, L.; Campforts, B.; Uwihirwe, J.; Dewitte, O. Interactions between deforestation, landscape rejuvenation, and shallow landslides in the North Tanganyika-Kivu rift region, Africa. *Earth Surf. Dynam.* **2021**, *9*, 445–462. [CrossRef]
10. Depicker, A.; Jacobs, L.; Mboga, N.; Smets, B.; Van Rompaey, A.; Lennert, M.; Wolff, E.; Michellier, C.; Dewitte, O.; Govers, G. Historical dynamics of landslide risk from population and forest-cover changes in the Kivu Rift. *Nat. Sustain.* **2021**, *4*, 965–974. [CrossRef]
11. The Ministry of Disaster Management and Refugee Affairs. *National Risk Atlas of Rwanda Electronic Version*; The Ministry of Disaster Management and Refugee Affairs: Kigali, Rwanda, 2015; pp. 44–56.
12. Ministry in Charge of Emergency Management. Annual Report 2016, Disaster Response and Recovery Unit Rwanda; 2016; pp. 1–4. Available online: https://www.minema.gov.rw/index.php?eID=dumpFile&t=f&f=77824&token=28ede27a12ae8ae92614e178eb1f6433967c3323 (accessed on 20 September 2024).
13. Ministry in Charge of Emergency Management. Disaster Effects Situation in 2018; 2019; pp. 1–9. Available online: https://www.minema.gov.rw/index.php?eID=dumpFile&t=f&f=77827&token=4baf6cc97a55675f3cb61ab0f87637b69e4ef70b (accessed on 20 September 2024).
14. Ministry in Charge of Emergency Management. Disaster Damages by Type of Disaster (01/01/2019-31/12/2019); 2020; pp. 1–4. Available online: https://www.minema.gov.rw/index.php?eID=dumpFile&t=f&f=77828&token=87be5c683ee8d16233eaf81a41790a104b437a0b (accessed on 20 September 2024).
15. Caine, N. The rainfall intensity-duration control of shallow landslides and debris flows. *Geogr. Ann.* **1980**, *62*, 23–27.
16. Crosta, G.B.; Frattini, P. Rainfall-induced landslides and debris flows. *Hydrol. Process.* **2008**, *22*, 473–477. [CrossRef]
17. Lee, M.L.; Ng, K.Y.; Huang, Y.F.; Li, W.C. Rainfall-induced landslides in Hulu Kelang area, Malaysia. *Nat. Hazards* **2014**, *70*, 353–375. [CrossRef]
18. Alsubal, S.; bin Sapari, N.; Harahap, I.S.H.; Al-Bared, M.A.M. A review on mechanism of rainwater in triggering landslide. *IOP Conf. Ser. Mater. Sci. Eng.* **2019**, *513*, 012009. [CrossRef]
19. Saito, H.; Nakayama, D.; Matsuyama, H. Relationship between the initiation of a shallow landslide and rainfall intensity—Duration thresholds in Japan. *Geomorphology* **2010**, *118*, 167–175. [CrossRef]
20. Peng, J.; Fan, Z.; Wu, D.; Zhuang, J.; Dai, F.; Chen, W.; Zhao, C. Heavy rainfall triggered loess-mudstone landslide and subsequent debris flow in Tianshui, China. *Eng. Geol.* **2015**, *186*, 79–90. [CrossRef]
21. De Falco, M.; Forte, G.; Marino, E.; Massaro, L.; Santo, A. UAV and field survey observations on the November 26th 2022 Celario flowslide, Ischia Island (Southern Italy). *J. Maps* **2023**, *19*, 2261484. [CrossRef]
22. Jaedicke, C.; Kleven, A. Long-term precipitation and slide activity in south-eastern Norway, autumn 2000. *Hydrol. Process.* **2008**, *22*, 495–505. [CrossRef]
23. Marques, R.; Zêzere, J.; Trigo, R.; Gaspar, J.; Trigo, I. Rainfall patterns and critical values associated with landslides in Povoação County (São Miguel Island, Azores): Relationships with the North Atlantic Oscillation. *Hydrol. Process.* **2008**, *22*, 478–494. [CrossRef]
24. Rahardjo, H.; Leong, E.C.; Rezaur, R.B. Effect of antecedent rainfall on pore-water pressure distribution characteristics in residual soil slopes under tropical rainfall. *Hydrol. Process.* **2008**, *22*, 506–523. [CrossRef]
25. Zhang, Z.; Zeng, R.; Meng, X.; Zhao, S.; Wang, S.; Ma, J.; Wang, H. Effects of changes in soil properties caused by progressive infiltration of rainwater on rainfall-induced landslides. *Catena* **2023**, *233*, 107475. [CrossRef]
26. Moeyersons, J. A Possible Causal Relationship between Creep and Sliding on Rwaza Hill, Southern Rwanda. *Earth Surf. Process. Landf.* **1989**, *14*, 597–614. [CrossRef]
27. Moeyersons, J. Les glissements de terrain au Rwanda occidental: Leurs causes et les possibilités de leur prévention. *Cah. ORSTOM Sér. Pédol* **1989**, *25*, 131–149. Available online: https://horizon.documentation.ird.fr/exl-doc/pleins_textes/cahiers/PTP/30465.PDF (accessed on 20 September 2024).
28. Bizimana, H.; Sonmez, O. Landslide Occurrences in the Hilly Areas of Rwanda, Their Causes and Protection Measures. *Disaster Sci. Eng.* **2015**, *1*, 1–7.
29. Kuradusenge, M.; Kumaran, S.; Zennaro, M. Rainfall-Induced Landslide Prediction Using Machine Learning Models: The Case of Ngororero District, Rwanda. *Int. J. Environ. Res. Public Health* **2020**, *17*, 4147. [CrossRef]
30. Nahayo, L.; Ndayisaba, F.; Karamage, F.; Nsengiyumva, J.B.; Kalisa, E.; Mind'je, R.; Mupenzi, C.; Li, L. Estimating Landslides Vulnerability in Rwanda Using Analytic Hierarchy Process and Geographic Information System. Integr. Environ. *Assess. Manag.* **2019**, *15*, 364–373.
31. Nsengiyumva, J.B.; Luo, G.; Amanambu, A.C.; Mind'je, R.; Habiyaremye, G.; Karamage, F.; Ochege, F.U.; Mupenzi, C. Comparing Probabilistic and Statistical Methods in Landslide Susceptibility Modeling in Rwanda/Centre-Eastern Africa. *Sci. Total Environ.* **2019**, *659*, 1457–1472. [CrossRef] [PubMed]
32. Ulvtorp, M. *Kallner Floods and Landslides in the Bakokwe Catchment, Rwanda*; Department of Building & Environmental Technology Lund University: Lund, Sweden, 2022; pp. 1–163.

33. Nsengiyumva, J.B.; Luo, G.; Nahayo, L.; Huang, X.; Cai, P. Landslide Susceptibility Assessment Using Spatial Multi-Criteria Evaluation Model in Rwanda. *Int. J. Environ. Res. Public Health* **2018**, *15*, 243. [CrossRef] [PubMed]
34. Monsieurs, E.; Jacobs, L.; Michellier, C.; Basimike Tchangaboba, J.; Ganza, G.B.; Kervyn, F.; Maki Mateso, J.-C.; Mugaruka Bibentyo, T.; Kalikone Buzera, C.; Nahimana, L.; et al. Landslide Inventory for Hazard Assessment in a Data-Poor Context: A Regional-Scale Approach in a Tropical African Environment. *Landslides* **2018**, *15*, 2195–2209. [CrossRef]
35. Nema, M.-L.; Saley Mahaman, B.; Diedhiou, A.; Mugabe, A. Local Perception and Adaptation Strategies to Landslide Occurrence in the Kivu Catchment of Rwanda. *Nat. Hazards Earth Syst. Sci. Discuss.* **2023**. [CrossRef]
36. Uwihirwe, J.; Hrachowitz, M.; Bogaard, T.A. Landslide Precipitation Thresholds in Rwanda. *Landslides* **2020**, *17*, 2469–2481. [CrossRef]
37. Dewitte, O.; Dille, A.; Depicker, A.; Kubwimana, D.; Maki Mateso, J.-C.; Mugaruka Bibentyo, T.; Uwihirwe, J.; Monsieurs, E. Constraining Landslide Timing in a Data-Scarce Context: From Recent to Very Old Processes in the Tropical Environment of the North Tanganyika-Kivu Rift Region. *Landslides* **2021**, *18*, 161–177. [CrossRef]
38. Rwanda Red cross on X. Available online: https://twitter.com/Rwandaredcross/status/993498780438802432 (accessed on 6 October 2023).
39. Funk, C.; Peterson, P.; Landsfeld, M.; Pedreros, D.; Verdin, J.; Shukla, S.; Husak, G.; Rowland, J.; Harrison, L.; Hoell, A.; et al. The Climate Hazards Infrared Precipitation with Stations—A New Environmental Record for Monitoring Extremes. *Sci. Data* **2015**, *2*, 150066. [CrossRef]
40. Fernandez-Alonso, M.; Cutten, H.; Waele, B.; Tack, L.; Tahon, A.; Baudet, D.; Barritt, S.D. The Mesoproterozoic Karagwe-Ankole Belt (Formerly the NE Kibara Belt): The Result of Prolonged Extensional Intracratonic Basin Development Punctuated by Two Short-Lived Far-Field Compressional Events. *Precambrian Res.* **2012**, *216–219*, 63–86. [CrossRef]
41. Baudet, D.; Hanon, M.; Lemonne, E.; Theunissen, K. Lithostratigraphie Du Domaine Sedimentaire de La Chaine Kibarienne Au Rwanda. *Ann. Soc. Geol. Belg.* **1988**, *112*, 225–246.
42. Theunissen, K.; Hanon, M.; Fernandez-Alonso, M. *Carte Géologique Du Rwanda Au 1/250.000*; Royal Museum for Central Africa: Tervuren, Belgium, 1991; Volume 1.
43. Ebinger, C.J.; Deino, A.L.; Drake, R.E.; Tesha, A.L. Chronology of Volcanism and Rift Basin Propagation: Rungwe Volcanic Province, East Africa. *J. Geophys. Res. Solid Earth* **1989**, *94*, 15785–15803. [CrossRef]
44. Smets, B.; Delvaux, D.; Ross, K.A.; Poppe, S.; Kervyn, M.; d'Oreye, N.; Kervyn, F. The Role of Inherited Crustal Structures and Magmatism in the Development of Rift Segments: Insights from the Kivu Basin, Western Branch of the East African Rift. *Tectonophysics* **2016**, *683*, 62–76. [CrossRef]
45. USGS Earthquake Lists, Maps, and Statistics. Available online: https://earthquake.usgs.gov/earthquakes/eventpage/us7000kxts/executive (accessed on 18 March 2024).
46. Petricec, V.; Lavreau, J.; Waleffe, A. Carte Lithologique Du Rwanda. Scale 1:250,000. *Inst. Géogr. Natl. Belg.* **1981**, *1*, G8431.C57.
47. European Space Agency. *Copernicus DEM—Global and European Digital Elevation Model (COP-DEM) [Dataset]*; European Space Agency: Paris, France, 2019. [CrossRef]
48. Muhire, I.; Ahmed, F.; Abutaleb, K.; Kabera, G. Impacts of Projected Changes and Variability in Climatic Data on Major Food Crops Yields in Rwanda. *Int. J. Plant Prod.* **2015**, *9*, 347–371.
49. National Land Authority (NLA); Digital Elevation Model (DEM). 10 m Resolution, Rwanda | Data | GeoHub. Available online: https://geohub.data.undp.org/data/00d5add9be37e465398b081683c3ec03 (accessed on 5 July 2024).
50. Rose, R. Slope Control on the Frequency Distribution of Shallow Landslides and Associated Soil Properties, North Island, New Zealand. *Earth Surf. Process. Landf.* **2013**, *38*, 356–371. [CrossRef]
51. Akiyama, K.; Uchida, T.; Mori, N.; Tamura, K.; Yamakoshi, T. The Role of Soil Thickness on Shallow Landslide Initiation. *Geophys. Res. Abstr.* **2009**, *11*, 7905.
52. Ho, J.-Y.; Lee, K.; Chang, T.-C.; Wang, Z.; Liao, Y.-H. Influences of Spatial Distribution of Soil Thickness on Shallow Landslide Prediction. *Eng. Geol.* **2011**, *124*, 38–46. [CrossRef]
53. Acharya, G.; Cochrane, T.A.; Davies, T.; Bowman, E. The Influence of Shallow Landslides on Sediment Supply: A Flume-Based Investigation Using Sandy Soil. *Eng. Geol.* **2009**, *109*, 161–169. [CrossRef]
54. Chang, K.-T. *Introduction to Geographic Information Systems*, 9th ed.; McGraw-Hill Education: New York, NY, USA, 2019; ISBN 978-1-259-92964-9;1-444.
55. Rooy, M. A Rainfall Anomaly Index Independent of Time and Space, Notos. *Weather Bur. S. Afr.* **1965**, *14*, 43–48.
56. Muñoz-Sabater, J.; Dutra, E.; Agustí-Panareda, A.; Albergel, C.; Arduini, G.; Balsamo, G.; Boussetta, S.; Choulga, M.; Harrigan, S.; Hersbach, H.; et al. ERA5-Land: A state-of-the-art global reanalysis dataset for land applications. *Earth Syst. Sci. Data* **2021**, *13*, 4349–4381. [CrossRef]
57. Gray, J.M.; Bishop, T.F.A.; Wilford, J.R. Lithology and soil relationships for soil modelling and mapping. *Catena* **2016**, *147*, 429–440. [CrossRef]
58. Huang, C.; Byrne, T.B.; Ouimet, W.B.; Lin, C.-W.; Hu, J.-C.; Fei, L.-Y.; Wang, Y.-B. Tectonic foliations and the distribution of landslides in the southern Central Range, Taiwan. *Tectonophysics* **2016**, *692*, 203–212. [CrossRef]
59. Taylor, R.G.; Howard, K.W.F. Post-Palaeozoic evolution of weathered landsurfaces in Uganda by tectonically controlled deep weathering and stripping. *Geomorphology* **1998**, *25*, 173–192. [CrossRef]

60. Burke, K.; Gunnell, Y. The African erosion surface: A continental-scale synthesis of geomorphology, tectonics, and environmental change over the past 180 million years. *Geol. Soc. Am. Mem.* **2008**, *201*, 66. [CrossRef]
61. Guillocheau, F.; Simon, B.; Baby, G.; Bessin, P.; Robin, C.; Dauteuil, O. Planation surfaces as a record of mantle dynamics: The case example of Africa. *Gondwana Res.* **2018**, *53*, 82–98. [CrossRef]
62. Rossi, G. Evolution des versants et mise en valeur agricole au Rwanda. *Ann. Géogr.* **1984**, *515*, 23–43. [CrossRef]
63. Wassmer, P.; Schwartz, D.; Gomez, C.; Ward, S.; Barrere, P. Geomorphology and sedimentary structures of Upper Pleistocene to Holoce alluvium within the Nyabarongo valley (Rwanda). Palaeo-climate and palaeo-environmental implications. *Geogr. Fis. Dinam. Quat.* **2013**, *36*, 199–210. [CrossRef]
64. Varnes, D.J. Slope movement types and processes. *Spec. Rep.* **1978**, *176*, 11–33.
65. Hungr, O.; Leroueil, S.; Picarelli, L. The Varnes Classification of Landslide Types, an Update. *Landslides* **2014**, *11*, 167–194. [CrossRef]
66. Bhattacharyya, S.; Sreekesh, S.; King, A. Characteristics of Extreme Rainfall in Different Gridded Datasets over India during 1983–2015. *Atmos. Res.* **2022**, *267*, 105930. [CrossRef]
67. Lei, X.; Xu, W.; Chen, S.; Yu, T.; Hu, Z.; Zhang, M.; Jiang, L.; Bao, R.; Guan, X.; Ma, M.; et al. How well does the ERA5 reanalysis capture the extreme climate events over China? Part I: Extreme Temperature. *Front. Environ. Sci.* **2022**, *10*, 921659. [CrossRef]
68. Tan, M.L.; Armanuos, A.M.; Ahmadianfar, I.; Demir, V.; Heddam, S.; Al-Areeq, A.M.; Abba, S.I.; Halder, B.; Cagan Kilinc, H.; Yaseen, Z.M. Evaluation of NASA POWER and ERA5-Land for Estimating Tropical Precipitation and Temperature Extremes. *J. Hydrol.* **2023**, *624*, 129940. [CrossRef]
69. Dutta, R.; Markonis, Y. Does ERA5-Land Capture the Changes in the Terrestrial Hydrological Cycle across the Globe? *Environ. Res. Lett.* **2024**, *19*, 024054. [CrossRef]
70. Siccard, V.; Lissak, C.; Gomez, C. Des instabilités de versant aux sources sédimentaires: Étude de la catastrophe géomorphologique du 5–6 juillet 2017 dans le bassin-versant du Chikugo (Kyūshū, Japon). *Géomorphologie* **2022**, *28*, 257–271. [CrossRef]
71. Khazai, B.; Sitar, N. Evaluation of Factors Controlling Earthquake-Induced Landslides Caused by Chi-Chi Earthquake and Comparison with the Northridge and Loma Prieta Events. *Eng. Geol.* **2004**, *71*, 79–95. [CrossRef]
72. Tang, C.; Zhu, J.; Qi, X.; Ding, J. Landslides Induced by the Wenchuan Earthquake and the Subsequent Strong Rainfall Event: A Case Study in the Beichuan Area of China. *Eng. Geol.* **2011**, *122*, 22–33. [CrossRef]
73. Sidle, R.; Ochiai, H. *Landslides: Processes, Prediction, and Land Use*; American Geophysical Union: Washington, DC, USA, 2006; p. 312. ISBN 978-0-87590-322-4.
74. Van Westen, C.J.; Castellanos Abella, E.A.; Kuriakose, S. Spatial Data for Landslide Susceptibility, Hazard, and Vulnerability Assessment: An Overview. *Eng. Geol.* **2008**, *102*, 112–131. [CrossRef]
75. Chok, Y.H.; Jaksa, M.; Kaggwa, W.; Griffiths, D. Assessing the Influence of Root Reinforcement on Slope Stability by Finite Elements. *Int. J. Geo-Eng.* **2015**, *6*, 12. [CrossRef]
76. Gonzalez-Ollauri, A.; Mickovski, S.B. Hydrological Effect of Vegetation against Rainfall-Induced Landslides. *J. Hydrol.* **2017**, *549*, 374–387. [CrossRef]
77. Zayadi, R.; Putri, C.; Irfan, M.; Kusuma, Z.; Leksono, A.; Yanuwiadi, B. Soil Reinforcement Modelling on a Hilly Slope with Vegetation of Five Species in the Area Prone to Landslide in Malang, Indonesia. *Environ. Res. Eng. Manag.* **2022**, *78*, 56–72. [CrossRef]
78. Iverson, R.M.; Denlinger, R.P. Flow of variably fluidized granular masses across three-dimensional terrain 1. Coulomb mixture theory. *J. Geoph. Res.* **2001**, *106*, 537–552. [CrossRef]
79. Iverson, R.M. The Physics of Debris Flows. *Rev. Geophys.* **1997**, *35*, 245–296. [CrossRef]
80. Liu, A.J.; Nagel, S.R. Jamming Is Not Just Cool Any More. *Nature* **1998**, *396*, 21–22. [CrossRef]
81. Mainsant, G.; Jongmans, D.; Chambon, G.; Larose, E.; Baillet, L. Shear-Wave Velocity as an Indicator for Rheological Changes in Clay Materials: Lessons from Laboratory Experiments. *Geophys. Res. Lett.* **2012**, *39*, L19301. [CrossRef]
82. Josserand, C.; Tkachenko, A.V.; Mueth, D.M.; Jaeger, H.M. Memory Effects in Granular Materials. *Phys. Rev. Lett.* **2000**, *85*, 3632–3635. [CrossRef]
83. Vassallo, R.; Grimaldi, G.M.; Di Maio, C. Pore water pressures induced by historical rain series in a clayey landslide: 3D modeling. *Landslides* **2015**, *12*, 731–744. [CrossRef]
84. Umbanhowar, P.; van Hecke, M. Force Dynamics in Weakly Vibrated Granular Packings. *Phys. Rev. E* **2005**, *72*, 030301. [CrossRef]
85. Lastakowski, H.; Géminard, J.-C.; Vidal, V. Granular Friction: Triggering Large Events with Small Vibrations. *Sci. Rep.* **2015**, *5*, 13455. [CrossRef]
86. Kappus, M.E.; Vernon, F.L. Acoustic signature of thunder from seismic records. *J. Geophys. Res.* **1991**, *96*, 10989–11006. [CrossRef]
87. Lin, T.L.; Langston, C.A. Infrasound from thunder: A natural seismic source. *Geophys. Res. Lett.* **2007**, *34*, L14304. [CrossRef]
88. Lin, T.L.; Langston, C.A. Thunder-induced ground motions: 1. Observations. *J. Geophys. Res.* **2009**, *114*, B04303. [CrossRef]
89. Lin, T.L.; Langston, C.A. Thunder-induced ground motions: 2. Site characterization. *J. Geophy. Res.* **2009**, *114*, B04304. [CrossRef]
90. Sorrells, G.C.; McDonald, J.A.; Herrin, E.; Der, Z.A. Earth motion caused by local atmospheric-pressure changes. *Geophys. J. Royal Astr. Soc.* **1971**, *26*, 83–98. [CrossRef]
91. Dybing, S.N.; Ringler, A.T.; Wilson, D.C.; Anthony, R.E. Characteristics and spatial variability of wind noise on near-surface broadland seismometers characteristics. *Bull. Seismol. Soc. Am.* **2019**, *109*, 1082–1098. [CrossRef]

92. Johnson, C.W.; Meng, H.; Vernon, F.; Ben-Zion, Y. Characteristics of ground motion generated by wind interaction with trees, structures, and other surface obstacles. *J. Geoph. Res. Solid Earth* **2019**, *124*, 8519–8539. [CrossRef]
93. Withers, M.M.; Aster, R.C.; Young, C.J.; Chael, E.P. High-frequency analysis of seismic background noise as a function of wind speed and shallow depth. *Bull. Seismol. Soc. Am.* **1996**, *86*, 1507–1515. [CrossRef]
94. De Angelis, S.; Bodin, P. Watching the wind: Seismic data contamination at long periods due to atmospheric pressure-field-induced tilting. *Bull. Seismol. Soc. Am.* **2012**, *102*, 1255–1265. [CrossRef]